ACS APPLIED BIO MATERIALS

www.acsabm.org Article

Two-Dimensional Metalloporphyrinic Framework Nanosheet-Based Dual-Mechanism-Driven Ratiometric Electrochemiluminescent Biosensing of Protein Kinase Activity

Guangyao Zhang,* Mengjie Li, Kun Yu, Huining Chai,* Shenghao Xu, Tailin Xu, Lijun Qu, and Xueji Zhang*

Cite This: *ACS Appl. Bio Mater.* 2021, 4, 1616–1623 Read Online

ACCESS | Metrics & More | Article Recommendations | Supporting Information

ABSTRACT: A dual-mechanism-driven ratiometric electrochemiluminescent (ECL) biosensor was developed for the ultrasensitive detection of protein kinase activity, which was based on a competitive catalytic reaction and resonance energy transfer (RET) by assembling gold nanoparticles (GNPs) on two-dimensional (2D) porphyrinic metal−organic framework (MOF) nanosheets. In this work, an ECL catalytic reaction competing for dissolved O_2 proceeded between 2D copper-based zinc porphyrinic MOF (Cu−TCPP(Zn)) nanosheets and luminol. Meanwhile, the cathodic ECL of singlet oxygen ($^1O_2$), derived from the electrocatalytic reaction of 2D Cu−TCPP(Zn), would be reduced by the assembled GNPs due to RET, while the anodic emission of luminol could be enhanced by GNPs with excellent electrocatalytic activity. With the detection of protein kinase A (PKA) as an example, this dual-mechanism-driven ECL biosensor exhibited a broad linear range (0.005−5.0 U mL^{-1}) and a sensitive detection limit (0.0037 U mL^{-1}). Compared with the traditional single-mechanism-driven sensing strategies, the developed dual-mechanism-driven ratiometric ECL biosensor may provide an effective method for the design of green and ultrasensitive ECL sensors.

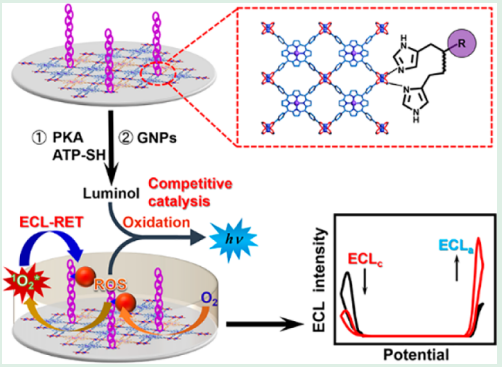

KEYWORDS: *protein kinase activity, electrochemiluminescence, two-dimensional porphyrinic metal−organic framework, dual-mechanism-driven mechanism, ratiometric biosensor*

INTRODUCTION

Protein kinases play crucial roles in signal transduction, metabolism, cell growth, and differentiation.[1−4] The deregulation of protein kinase activities may lead to a series of serious diseases including diabetic complications, cancers, and Alzheimer's disease.[5−7] Therefore, accurate identification of the kinase activities and screening of their potential inhibitors are of great importance for elucidating the signal transduction pathways, drug discoveries, targeted diagnosis, and therapies.

Up to now, a growing interest has emerged in developing various signal transduction pathways and analytical technologies for protein kinase activity detection. Generally, most signal transduction pathways relying on catalytic reactions,[8,9] surface charge change,[10] resonance energy transfer (RET),[11,12] and charge transfer[13] have been widely used for protein kinase activity biosensing studies. However, most of them are driven by a single sensing mechanism, resulting in low detection sensitivity and limited sensing performance.[14] And multiple-mechanism-driven sensors for protein kinase activity analysis have rarely been reported. Developing signal transduction strategies driven by multiple mechanisms would provide a new approach to further improve the analytical performance of protein kinase biosensors. Additionally, compared with several existing techniques such as ^{32}P radioactivity,[15] mass spectrometry (MS),[16] Raman spectroscopy,[17] fluorimetry,[18,19] colorimetry,[20] and electrochemical sensing,[21] an electrochemiluminescent (ECL) approach has aroused special attention because of its simple operation, low cost, low background noise, and high sensitivity.[22,23] To date, the enhanced ECL sensing strategies based on quantum dots (QDs) or metal nanoparticles are extensively utilized for protein kinase A (PKA) biosensors.[24,25] Although these methods could exhibit excellent analytical performance, the ECL sensing systems always need to introduce a coreactant, such as hydrogen peroxide (H_2O_2) to enhance the luminescence response. However, H_2O_2 tends to decompose at room temperature, resulting in poor stability and reproducibility of biosensors.[26,27] Therefore, novel sensing

Received: November 9, 2020
Accepted: January 19, 2021
Published: January 26, 2021

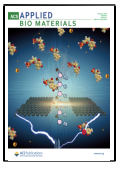

https://dx.doi.org/10.1021/acsabm.0c01453
ACS Appl. Bio Mater. 2021, 4, 1616–1623

Scheme 1. Fabricated Process of the 2D Cu−TCPP(Zn)-Based Dual-Mechanism-Driven Ratiometric ECL Biosensor for the PKA Assay

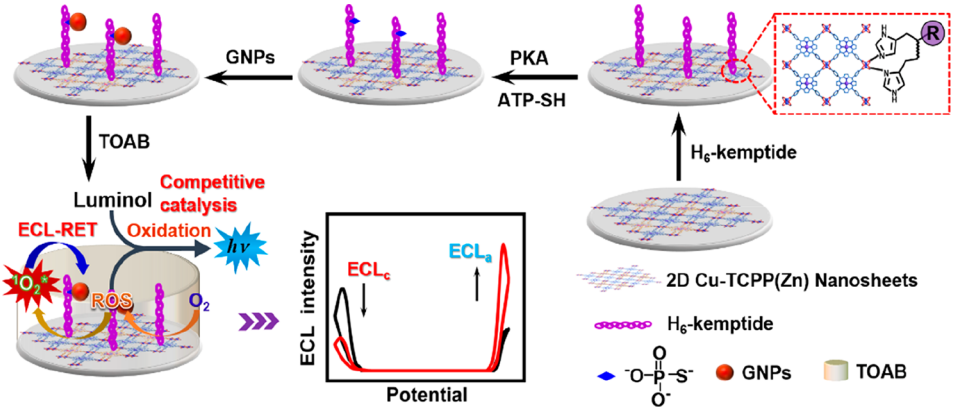

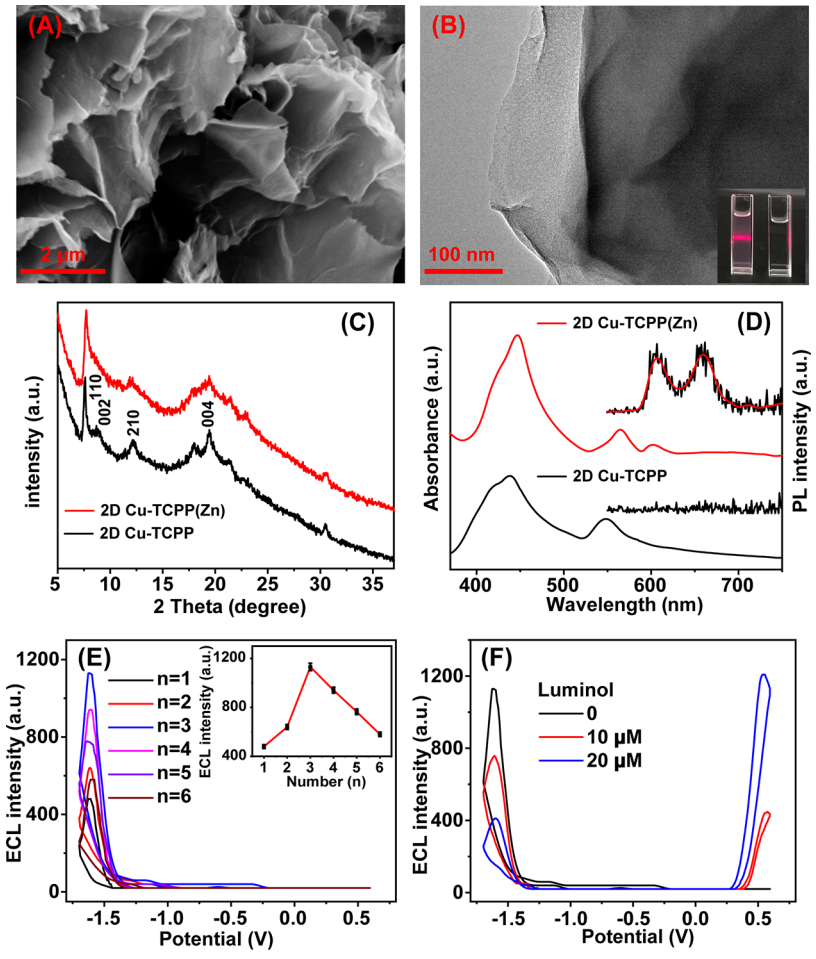

Figure 1. (A) SEM image and (B) TEM image of 2D Cu−TCPP(Zn) nanosheets. (C) PXRD patterns for 2D Cu−TCPP and 2D Cu−TCPP(Zn) nanosheets. (D) UV−vis absorption and PL emission (λ_{ex} = 430 nm) spectra of 2D Cu−TCPP(Zn) nanosheets. (E) ECL−potential curves of the GCE/(2D Cu−TCPP(Zn))$_n$/TOAB (n = 1−6). Inset E: Effect of films on the ECL responses. (F) ECL−potential curves of the GCE/2D Cu−TCPP(Zn)/TOAB at different concentrations of luminol.

strategies and green, stable ECL systems for the PKA assay are still in high demand.

Porphyrin-based ECL systems involving singlet oxygen ($^1O_2$) have been previously reported.[28−30] In particular, porphyrinic metal−organic frameworks (MOFs), composed of porphyrins or their derivative ligands, have been extensively applied for photoelectrochemical biosensing, because they possess more remarkable chemical stability and are prone to biofunctionalization compared with porphyrin monomers.[31−33] More recently, our group reported a novel competitive ECL mechanism between zirconium-based metalloporphyrinic MOF nanoparticles and luminol for ratio sensing of polynucleotide kinase (PNK) activity,[34] which is quite beneficial to the development of green and ultrasensitive

https://dx.doi.org/10.1021/acsabm.0c01453
ACS Appl. Bio Mater. 2021, 4, 1616−1623

ECL biosensors. Moreover, in comparison with the three-dimensional (3D) MOF crystals, two-dimensional (2D) MOF nanosheets, as a new type of 2D nanomaterials, have attracted increasing attention for gas separation, catalysis, and sensing because of their large surface area and highly exposed active sites.[35−37]

With all of this in mind, we propose to combine the competitive catalytic reaction with RET and apply them into the ECL biosensing interface by assembling gold nanoparticles (GNPs) on the 2D Cu-based zinc porphyrinic MOF (Cu−TCPP(Zn)) nanosheets. As shown in Scheme 1, the oligohistidine tag (His-tag) kemptide (H_6-kemptide) was immobilized on 2D Cu−TCPP(Zn) nanosheets via coordination binding between the His-tag peptides and unsaturated copper sites, and the PKA assay was realized by the dual-mechanism-driven ECL ratio biosensor with a lower detection limit compared with previous methods. This study opens a general avenue to expand the applications of 2D porphyrinic MOFs and gives a new way for further development of a green and ultrasensitive ECL biosensing system.

EXPERIMENTAL SECTION

Materials and Apparatus. All the reagents, materials, and apparatus used in this work are provided in the Supporting Information.

Synthesis of 2D MOF Nanosheets. The 2D MOF nanosheets were prepared by a previously reported method.[38] Briefly, 10 mg of tetrakis(4-carboxyphenyl)porphyrin (TCPP) or zinc(II) tetrakis(4-carboxyphenyl)porphyrin (TCPP(Zn)), 30 mg of $Cu(NO_3)_2{\cdot}3H_2O$, and 280 mg of polyvinylpyrrolidone (PVP) were ultrasonically dissolved in 10 mL of DMF and heated at 90 °C for 5 h in an oven. Then, the mixture was cooled to room temperature and centrifuged to obtain a dark purple rod-shaped precipitate, which was washed multiple times with ethanol, and 2D Cu−TCPP and Cu−TCPP(Zn) nanosheets were obtained, respectively.

Fabrication of the PKA Biosensor. Generally, the polished glass carbon electrode (GCE) was used as the working substrate electrode. Then, the GCE/2D MOFs were obtained by using the Langmuir-Schafer transfer method (Scheme S1).[39] As illustrated in Scheme 1, the obtained GCE/2D Cu−TCPP(Zn) was incubated with 20 μL of H_6-kemptide (200 μM) for 12 h at 25 °C. After being rinsed with buffer solution, the modified electrode was further reacted with different concentrations of PKA and ATP-SH at 37 °C for 1 h to perform PKA-catalyzed peptide phosphorylation. After rinsing, 20 μL of GNP solution was dispersed onto the above-modified GCE for 1 h to adsorb GNPs onto the phosphorylated peptide-modified electrode surface. After the nonspecific GNPs were removed by washing, the surfactant, tetraoctylammonium bromide (TOAB, 5 μL, 10 mM), was coated on the above-modified electrode and dried at room temperature, and the ratiometric PKA biosensor was implemented to collect ECL signals in HEPES (10 mM, pH 7.4), 0.1 M KCl containing 10 μM luminol.

Inhibition Assay. Ellagic acid and tyrphostin AG 1478 were selected as typical models for protein kinase inhibition. Different concentrations of kinase inhibitors were introduced into 5 U mL^{-1} of PKA reaction buffer, measured by the same experimental procedures for PKA detection described above.

PKA Assay in Cell Lysates. Diluted HeLa cell extracts (1%) were added to the PKA assay solution by using the same test procedures for the PKA assay described above.

RESULTS AND DISCUSSION

Characterization and ECL Investigation of the 2D Cu−TCPP(Zn) Nanosheets. 2D Cu−TCPP(Zn) nanosheets were synthesized by using $Cu(NO)_3{\cdot}3H_2O$, ZnTCPP, and PVP via a bottom-up approach.[38] As illustrated in Scheme S2, the surfactant molecule, PVP, can adhere to MOF surface and play a prominent part in the anisotropic growth of Cu−TCPP(Zn), thus forming 2D Cu−TCPP(Zn) nanosheets. The 2D Cu−TCPP(Zn) nanosheets show well-defined ultrathin sheet-like structures from scanning electron microscopy (SEM) and transmission electron microscopy (TEM) images (Figure 1A,B). When a red laser passes through it, the colloidal structure of 2D-Cu−TCPP(Zn) nanosheets is confirmed, as the 2D MOF exhibits a distinct Tyndall effect (inset in Figure 1B). Moreover, the powder X-ray diffraction (PXRD) pattern of 2D Cu−TCPP(Zn) nanosheets gives three obvious peaks indexed as (110), (210), (004), which are consistent with those of 2D Cu−TCPP nanosheets[38] and confirm the crystalline feature of 2D MOF (Figure 1C). The UV−vis absorption and photoluminescence (PL) emission spectra of 2D Cu−TCPP and Cu−TCPP(Zn) nanosheets are shown in Figure 1D. The UV−vis absorption spectrum of 2D Cu−TCPP nanosheets exhibits a metal-coordination-induced Q-band absorption at 548 nm, a Soret band at 420 nm, and an accompanying shoulder at 438 nm, due to the J-aggregation of the MOF nanosheets.[40] For the 2D Cu−TCPP(Zn), a typical Soret band (447 nm) tailing with two Q-bands (565 and 603 nm) could be observed, which is in line with that of ZnTCPP,[41] validating the successful assembly of ZnTCPP units in 2D MOFs. Meanwhile, compared with the quenched fluorescence spectrum of 2D Cu−TCPP nanosheets derived from photoinduced electron transfer (PET) induced by copper coordination,[38] the PL emission spectrum of 2D Cu−TCPP(Zn) nanosheets shows two peaks at 607 and 660 nm, which indicates that both ground and excited states of porphyrin are affected by the zinc coordination. Therefore, 2D Cu−TCPP(Zn) nanosheets are similar to other 2ZnTCPP-based MOFs, possessing photoelectrochemical characteristics of the latter.

Moreover, the 2D Cu−TCPP(Zn) nanosheets may display the ECL catalytic activity. First, it is crucial for ECL study to fabricate 2D nanofilms with controllable thickness.[42−44] In order to verify it, the GCE/$(2D\ Cu{-}TCPP(Zn))_n$ (n = 1−6, number of deposition cycles) electrodes were obtained by employing the Langmuir-Schafer transfer method (Scheme S1). Moreover, the ECL behaviors of 2D Cu−TCPP(Zn) were investigated by using surfactant TOAB activated GCE. As shown in Figure 1E, an obvious cathodic emission peak was observed at −1.55 V, derived from $^1O_2$ generated by electrocatalytic reaction of 2D Cu−TCPP(Zn), and the ECL intensity increased with n up to 3. However, if n further increased from 3 to 6, the ECL intensity decreased, probably because the diffusion of dissolved O_2 to the zinc porphyrin active center was limited with the increased thickness of the MOF nanosheet film. Therefore, the GCE/$(2D\ Cu{-}TCPP(Zn))_3$ electrode was used as an ideal ECL platform for biosensing. Additionally, the ECL−time response of 2D Cu−TCPP(Zn) in aqueous media displayed constant and stable signals in the process of continuous cathodic potential scanning (Figure S1), suggesting the excellent cathodic ECL stability, which was attributed to the interlaminar pore structure of dissolved oxygen enriched MOF films. Second, the ECL behavior of the 2D Cu−TCPP(Zn)−luminol system was investigated. As shown in Figure 1F, the cathodic emission from $^1O_2$ decreased, and the anodic emission of luminol enhanced with the increasing amounts of luminol from 0 to 20 μM. The ratiometric ECL responses suggest that a competitive reaction involving dissolved O_2 proceeds between 2D Cu−

https://dx.doi.org/10.1021/acsabm.0c01453
ACS Appl. Bio Mater. 2021, 4, 1616−1623

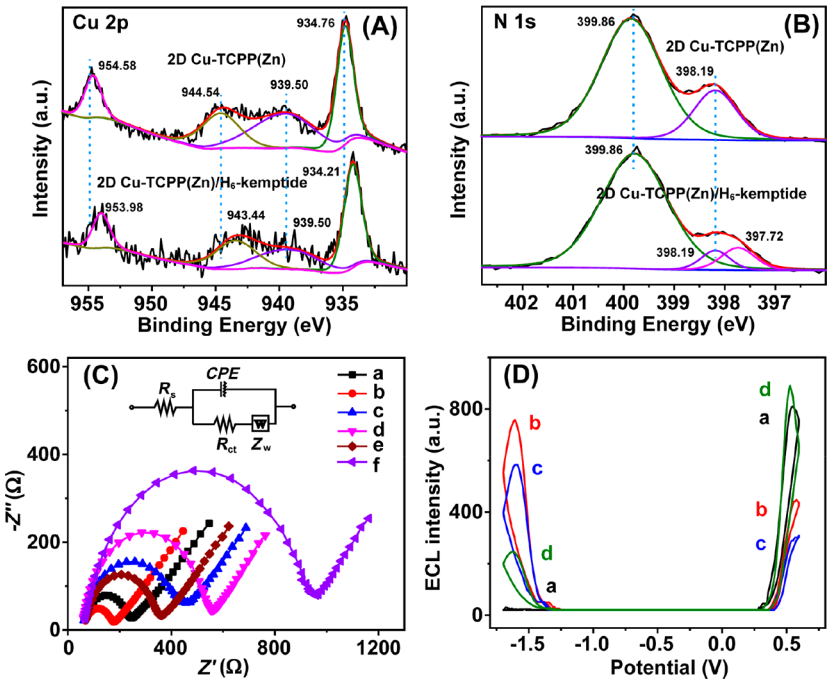

Figure 2. High-resolution XPS response of Cu 2p (A) and N 1s (B) core energy levels for 2D Cu−TCPP(Zn) and 2D Cu−TCPP(Zn)/H_6-kemptide. (C) Nyquist plots of EIS after each step of assembly: (a) bare GCE, (b) GCE/2D Cu−TCPP(Zn), (c) GCE/2D Cu−TCPP(Zn)/H_6-kemptide, (d) GCE/2D Cu−TCPP(Zn)/H_6-kemptide/phosphorylated H_6-kemptide, (e) modified electrode after assembly of GNPs, and (f) GCE/2D Cu−TCPP(Zn)/H_6-kemptide/phosphorylated H_6-kemptide/GNPs/TOAB. Inset A: the equivalent circuit. Electrolytes: 5 mM $Fe(CN)_6^{4-/3-}$ in 0.1 M KCl solution. (D) ECL−potential curves of the (a) GCE/TOAB, (b) GCE/2D Cu−TCPP(Zn)/TOAB, (c) GCE/2D Cu−TCPP(Zn)/H_6-kemptide/TOAB, and (d) GCE/2D Cu−TCPP(Zn)/H_6-kemptide/phosphorylated H_6-kemptide after assembly of GNPs, modified by TOAB.

TCPP(Zn) and luminol. Meanwhile, we studied the effect of dissolved O_2 on this competitive complex system. As shown in Figure S2A, no ECL signal was observed in the N_2-saturated environment. With an increasing dissolved O_2 concentration, the anodic and cathodic ECL responses gradually increased, demonstrating that dissolved O_2 was involved in the competitive reaction and boosted the cathodic and anodic emission. The competitive ECL system with continuous voltammetric scanning displayed stable dual-potential emission responses (Figure S2B), indicating that the 2D Cu−TCPP(Zn)−luminol competitive ECL system exhibits excellent stability. And the possible mechanism of the dual-potential ECL system is illustrated in eqs S1−10. Thus, the proposed 2D Cu−TCPP(Zn)−luminol competitive ECL ratiometric approach is expected to be used for biosensing and bioassay accurately and sensitively.

Construction and Feasibility of the ECL Biosensor. Based on the intrinsic coordination binding of copper and His-tag peptides,[45] H_6-kemptide was assembled on the 2D Cu−TCPP(Zn) nanosheet surface. X-ray photoelectron spectroscopy (XPS) experiments were used to identify valence states of elements. As shown in Figure S3A,B, besides the peaks of C, N, O, and Cu, the Zn 2p peaks of 1021.72 and 1044.50 eV were observed in the spectrum of 2D Cu−TCPP(Zn) nanosheets, derived from the zinc ion in the porphyrin ring. Meanwhile, the coordination between the MOF nanosheets and H_6-kemptide was investigated by comparing the high-resolution Cu 2p and N 1s spectra of 2D Cu−TCPP(Zn) and 2D Cu−TCPP(Zn)/H_6-kemptide. As shown in Figure 2A, the high-resolution Cu 2p spectra fit perfectly with a line centered at binding energies of 954.58, 944.54, 939.50, and 934.76 eV; in contrast, the peaks appeared at 953.98, 943.44, 939.50, and 934.50 eV after the H_6-kemptide assembly. After the H_6-kemptide-functionalized complex was formed, the typical binding energy of Cu is obviously transferred to a lower state. It is seen that the N 1s spectrum of 2D MOF nanosheets contains two peaks at 399.86 and 398.19 eV, derived from pyridinic and pyrrolic moieties of the zinc porphyrin ring.[46] After H_6-kemptide assembly, the XPS N 1s shows one more peak at 397.72 eV by using the curve fitting procedure, which might be attributed to the Cu−N bonding and amino nitrogen in kemptide (Figure 2B). Therefore, the results suggested that 2D Cu−TCPP(Zn) and H_6-kemptide are well-combined by strong interactions.

Then, the assembly process of the designed ECL biosensor was further studied by electrochemical impedance spectroscopy (EIS). The semicircle diameter of the Nyquist plot is associated with the charge-transfer resistance (denoted as R_{ct}) at the electrode/solution interface. As shown in Figure 2C, compared with bare GCE, the semicircle diameter of the GCE/$(2D\ Cu{-}TCPP(Zn))_3$ electrode decreased from 198 to 153 Ω (Figure 2C, curve b), which benefited from the charge-transfer capacity improved by porphyrinic MOFs.[32,33] With the successive assembling of the H_6-kemptide and the phosphorylation of the peptide by PKA and ATP-SH, the R_{ct} increased gradually (Figure 2C, curves c and d), indicating the poor conductivity of the biomolecules. However, the R_{ct} value reduced after GNPs were captured on the electrode via a Au−S bond (Figure 2C, curve e), owing to the excellent conductivity of GNPs. Notably, the addition of the surfactant TOAB caused a further increase on the R_{ct} value (Figure 2C, curve f). Additionally, Figure 2D shows the ECL behavior of four different working electrodes in the electrolyte containing luminol. For GCE/TOAB, only a strong anodic emission from

https://dx.doi.org/10.1021/acsabm.0c01453
ACS Appl. Bio Mater. 2021, 4, 1616−1623

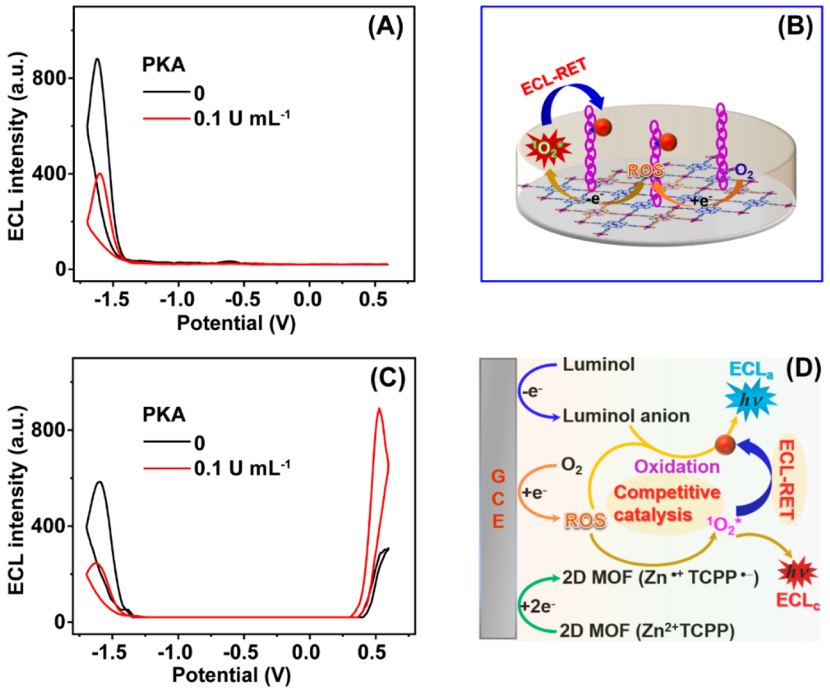

Figure 3. (A) ECL−potential curves of biosensor recorded in pH 7.4 HEPES solution without luminol, and (B) schematic illustration for ECL-RET between $^1O_2$ and GNPs. (C) ECL−potential curves of biosensor recorded in pH 7.4 HEPES solution with 10 μM luminol, and (D) schematic illustration for dual-mechanism-driven ECL system (ECL-RET and competitive catalysis).

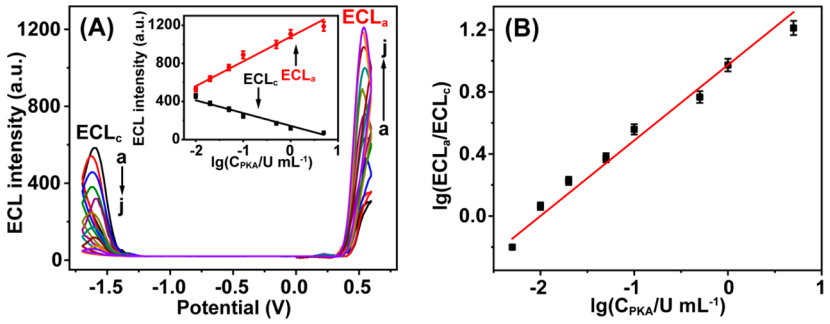

Figure 4. (A) ECL−potential curves of the biosensor for different concentrations of PKA: (a−j) 0, 0.005, 0.01, 0.02, 0.05, 0.1, 0.5, 1.0, 5.0, and 10.0 U mL^{-1}. Inset A: calibration curves. (B) Calibration plot of lg(ECL_a/ECL_c) − lg(C_{PKA}).

luminol was observed (Figure 2D, curve a). After 2D MOF films were assembled on the GCE, a marked decrease of the anodic emission peak and a strong cathodic emission peak were observed (Figure 2D, curve b), because the introduction of 2D Cu−TCPP(Zn) nanosheets leads to a competitive ECL performance. With the H_6-kemptide assembled through the coordination between His-tags and Cu−O clusters, the modified electrode exhibited both cathodic and anodic ECL intensity, which decreased (Figure 2D, curve c) as H_6-kemptide blocked interfacial electron transfer. However, after adsorbing GNPs onto the electrode surface, the cathodic ECL intensity decreased by 58.1%, while the anodic ECL peak of luminol increased by 195.2% (Figure 2D, curve d). Thus, both EIS and ECL measurement manifested the successful construction of the PKA biosensor.

Mechanism of ECL Biosensor. The dual-mechanism-driven ratiometric ECL biosensing strategy mainly depends on the competitive catalytic reaction and RET. To verify this, first, we explored the ECL-RET between $^1O_2$ and GNPs. When peptides were modified to the 2D Cu−TCPP(Zn) electrode surface and further phosphorylated in the presence of 0.1 U mL^{-1} of PKA and 60 μM ATP-SH, the GNPs were assembled onto the modified electrode surface. In the ECL biosensing system without luminol, the cathodic ECL from $^1O_2$ significantly decreased by 54.4% (Figure 3A), indicating that the assembled GNPs can quench the luminescence from $^1O_2$. Just as many luminophores have RET with GNPs in close proximity based on the necessary band overlap for efficient energy transfer,[24] the cathodic ECL of $^1O_2$, derived from electrocatalytic reaction of 2D Cu−TCPP(Zn), could be decreased by the assembled GNPs due to ECL-RET (Figure 3B). Next, we introduced the RET mechanism into the 2D MOF−luminol competitive ECL system. As shown in Figure 3C, a ratio response occurs at the ECL sensing interface; the cathodic ECL intensity of $^1O_2$ significantly decreased by 57.8%, while the anodic emission peak of luminol increased by 66.1%. It suggests that the cathodic ECL from $^1O_2$ can be decreased by closely contacting GNPs due to RET, while the anodic ECL from luminol can be enhanced by GNPs with excellent electrocatalytic activity in this competitive system (Figure 3D). It is expected that the ECL-RET and competitive catalytic reaction will be more remarkable as the PKA

https://dx.doi.org/10.1021/acsabm.0c01453
ACS Appl. Bio Mater. 2021, 4, 1616−1623

concentration increases in the biosensing system. As a result, the anodic ECL intensity will be stronger, and the cathodic ECL intensity will be weaker, that is, this dual-mechanism-driven ECL ratiometric approach can be employed for ultrasensitive detection of PKA activity.

Biosensing Performance of PKA Assay. After optimization of the detection conditions (peptide concentration and ATP-SH concentration) (Figure S4), the proposed dual-mechanism-driven ECL biosensor was used to detect PKA activity. As shown in Figure 4A, the anodic emission of luminol increased gradually with the concentration of PKA, while the cathodic ECL intensity decreased simultaneously, indicating the good response ability of the biosensor. The anodic or cathodic ECL intensity was dependent on the logarithm of the PKA concentration ranging from 0.01 to 5.0 U mL^{-1} (inset of Figure 4A). And the limits of detection (LODs) of these two ECL responses were estimated to be 0.0072 and 0.0093 U mL^{-1}, respectively, corresponding to a signal-to-noise ratio (S/N) of 3. On the other hand, the calibration curve in the Figure 4B demonstrated that the logarithm of the ratio of anodic to cathodic ECL intensity (ECL_a/ECL_c) was linear to the logarithm of PKA concentration ranging from 0.005 to 5.0 U mL^{-1}, $lg(ECL_a/ECL_c) = 0.9737 + 0.4867\ lgC_{PKA}$, with a correlation coefficient of $R^2 = 0.9890$. The LOD was estimated to be 0.0037 U mL^{-1}. Obviously, the comparison results indicate that this dual-potential ECL ratiometric method exhibits great superiority including sensitivity and a wider linear detection range. Moreover, other conventional single-mechanism-driven PKA assay methods are listed in Table S1 for comparison with the proposed ECL biosensor. The excellent analytical performance of the proposed biosensor may be ascribed to the highly efficient dual-mechanism-driven ECL process. Additionally, after 10 independent tests, the proposed biosensor exhibited satisfactory reproducibility with a variation coefficient of 5.34%. Meanwhile, the stability of the proposed biosensor was also examined (Figure S5). After the biosensor was measured upon 10 cycles of voltammetric scanning between 0.7 and 1.7 V, no apparent change in ECL signal was observed with a relative standard deviation (RSD) of 0.42%, demonstrating the excellent cyclic stability for the PKA assay.

Inhibition Assay. Kinase inhibitors can regulate kinase activity and become potential drugs, which have important significance in disease diagnosis and clinical therapy. Therefore, kinase inhibitor screening has attracted increasing interest. To evaluate the inhibition effects, the assay procedure above was implemented with different concentrations of kinase inhibitors. Ellagic acid, a well-recognized efficient PKA inhibitor because of its cell-permeable antioxidation and anticarcinogenic characteristics,[47] was used as a model inhibitor. The curve a of Figure 5 shows the relationship between the ellagic acid concentration and $lg(ECL_a/ECL_c)$. After calculation, the half-maximal inhibition value (IC_{50}) of ellagic acid was 1.15 μM, comparable with the previous reports.[13,48] Additionally, as a tyrosine kinase inhibitor, tyrphostin AG 1478 was used to compare the inhibition effects. The ECL responses exhibited no obvious trend with a tyrphostin AG 1478 concentration increase (Figure 5, curve b). These results confirmed the constructed biosensor was promising for screening PKA inhibitors.

Application in Real Sample Analysis. To demonstrate the applicability of the proposed biosensing platform, we performed the experiment in complex biological samples by detecting PKA in the buffer containing HeLa cell extracts (1%, v/v). The recoveries were calculated to be 96, 106, 108% for measurement of 0.05, 0.1, and 1 U mL^{-1} of PKA (Table S2), and the corresponding RSDs were around 3.05, 3.26, and 3.53%. The acceptable recoveries and low RSDs suggest that the proposed ECL biosensor can ensure the accuracy and reliability of PKA assay, which holds great prospects for clinical examination and biomedical research.

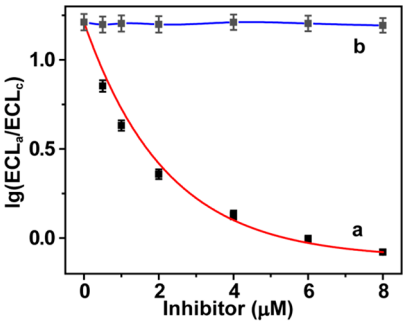

Figure 5. Inhibition effects of (a) ellagic acid and (b) tyrphostin AG 1478 on PKA activity. The concentrations of PKA and ATP-SH are 5 U mL^{-1} and 1 mM, respectively.

CONCLUSIONS

In summary, we have presented a dual-mechanism-driven ratiometric ECL strategy for an ultrasensitive PKA assay that unitized a competitive catalytic reaction and RET by assembling GNPs on 2D Cu−TCPP(Zn) nanosheets. The 2D MOF exhibits competitive ECL behavior involving dissolved O_2 in the presence of luminol, resulting in a dual-potential ratiometric ECL response. Additionally, the closely contacted GNPs assembled on the 2D Cu−TCPP(Zn) nanosheets by thiophosphorylation can not only quench the cathodic ECL from $^1O_2$ due to RET but also act as electrocatalysts to enhance the anodic emission of luminol. On this basis, compared to the conventional single-mechanism-driven biosensors, the proposed dual-mechanism-driven ECL biosensor exhibited better detection sensitivity and green sustainability. Furthermore, this developed approach could be utilized in kinase activity detection and potential inhibitor screening in complex biological samples, bearing a promising future in clinical diagnostics and drug discovery.

ASSOCIATED CONTENT

Supporting Information

The Supporting Information is available free of charge at https://pubs.acs.org/doi/10.1021/acsabm.0c01453.

Materials and apparatus; supplementary schemes, ECL of 2D Cu−TCPP(Zn), possible mechanism of the 2D Cu−TCPP(Zn)−luminol competitive ECL system, XPS, optimization of detection conditions, stability of the PKA assay, and Tables S1 and S2 (PDF)

AUTHOR INFORMATION

Corresponding Authors

Guangyao Zhang − *Intelligent Wearable Engineering Research Center of Qingdao, Research Center for Intelligent and Wearable Technology, College of Textiles and Clothing, State Key Laboratory of Bio-Fibers and Eco-Textiles, Qingdao University, Qingdao 266071, China;* orcid.org/0000-0002-7159-5166; Email: gyzhang@qdu.edu.cn

https://dx.doi.org/10.1021/acsabm.0c01453
ACS Appl. Bio Mater. 2021, 4, 1616−1623

Huining Chai − *School of Environmental and Municipal Engineering, Qingdao University of Technology, Qingdao 266033, China;* orcid.org/0000-0002-7267-2952; Email: chaihuining@qut.edu.cn

Xueji Zhang − *Intelligent Wearable Engineering Research Center of Qingdao, Research Center for Intelligent and Wearable Technology, College of Textiles and Clothing, State Key Laboratory of Bio-Fibers and Eco-Textiles, Qingdao University, Qingdao 266071, China; School of Biomedical Engineering, Health Science Center, Shenzhen University, Shenzhen 518060, China;* orcid.org/0000-0002-0035-3821; Email: zhangxueji@szu.edu.cn; Fax: +86-532-85953358

Authors

Mengjie Li − *Intelligent Wearable Engineering Research Center of Qingdao, Research Center for Intelligent and Wearable Technology, College of Textiles and Clothing, State Key Laboratory of Bio-Fibers and Eco-Textiles, Qingdao University, Qingdao 266071, China*

Kun Yu − *Intelligent Wearable Engineering Research Center of Qingdao, Research Center for Intelligent and Wearable Technology, College of Textiles and Clothing, State Key Laboratory of Bio-Fibers and Eco-Textiles, Qingdao University, Qingdao 266071, China*

Shenghao Xu − *Key Laboratory of Optic-electric Sensing and Analytical Chemistry for Life Science, MOE, Qingdao University of Science and Technology, Qingdao 266042, China;* orcid.org/0000-0003-3908-1525

Tailin Xu − *School of Biomedical Engineering, Health Science Center, Shenzhen University, Shenzhen 518060, China;* orcid.org/0000-0003-4037-2856

Lijun Qu − *Intelligent Wearable Engineering Research Center of Qingdao, Research Center for Intelligent and Wearable Technology, College of Textiles and Clothing, State Key Laboratory of Bio-Fibers and Eco-Textiles, Qingdao University, Qingdao 266071, China;* orcid.org/0000-0002-7951-7533

Complete contact information is available at: https://pubs.acs.org/10.1021/acsabm.0c01453

Notes

The authors declare no competing financial interest.

■ ACKNOWLEDGMENTS

This work was supported by the Natural Science Foundation of Shandong Province (No. ZR2020QB092), the National Natural Science Foundation of China (Grant Nos. 21801158, 21727815), the National Key R&D Program of China (No. 2017YFB0309000), the State Key Laboratory of Bio-Fibers and Eco-Textiles (Qingdao University, Nos. ZKT23, KF2020201, GZRC202025), and the Key Laboratory of Optic-electric Sensing and Analytical Chemistry for Life Science (Qingdao University of Science and Technology, No. OESACLS202007).

■ REFERENCES

(1) van der Geer, P.; Hunter, T.; Lindberg, R. A. Receptor Protein-Tyrosine Kinases and Their Signal Transduction Pathways. *Annu. Rev. Cell Biol.* **1994**, *10*, 251−337.

(2) Whiteman, E. L.; Cho, H.; Birnbaum, M. J. Role of Akt/protein kinase B in metabolism. *Trends Endocrinol. Metab.* **2002**, *13*, 444−451.

(3) Zhang, H.; Buckley, N. E.; Gibson, K.; Spiegel, S. Sphingosine Stimulates Cellular Proliferation via a Protein Kinase C-independent Pathway. *J. Biol. Chem.* **1990**, *265*, 76−81.

(4) Newton, K.; Dugger, D. L.; Wickliffe, K. E.; Kapoor, N.; de Almagro, M. C.; Vucic, D.; Komuves, L.; Ferrando, R. E.; French, D. M.; Webster, J.; Roose-Girma, M.; Warming, S.; Dixit, V. M. Activity of Protein Kinase RIPK3 Determines Whether Cells Die by Necroptosis or Apoptosis. *Science* **2014**, *343*, 1357−1360.

(5) Geraldes, P.; King, G. L. Activation of Protein Kinase C Isoforms and Its Impact on Diabetic Complications. *Circ. Res.* **2010**, *106*, 1319−1331.

(6) Li, M.; Xiong, Y.; Lu, W.; Wang, X.; Liu, Y.; Na, B.; Qin, H.; Tang, M.; Qin, H.; Ye, M.; Liang, X.; Qing, G. Functional Nanochannels for Sensing Tyrosine Phosphorylation. *J. Am. Chem. Soc.* **2020**, *142*, 16324−16333.

(7) Cohen, P. Protein Kinases — The Major Drug Targets of The Twenty-First Century? *Nat. Rev. Drug Discovery* **2002**, *1*, 309−315.

(8) Yan, Z.; Wang, F.; Deng, P.; Wang, Y.; Cai, K.; Chen, Y.; Wang, Z.; Liu, Y. Sensitive Electrogenerated Chemiluminescence Biosensors for Protein Kinase Activity Analysis Based on Bimetallic Catalysis Signal Amplification and Recognition of Au and Pt Loaded Metal-Organic Frameworks Nanocomposites. *Biosens. Bioelectron.* **2018**, *109*, 132−138.

(9) Zhang, G.-Y.; Cai, C.; Cosnier, S.; Zeng, H.-B.; Zhang, X.-J.; Shan, D. Zirconium−Metalloporphyrin Frameworks as a Three-in-One Platform Possessing Oxygen Nanocage, Electron Media, and Bonding Site for Electrochemiluminescence Protein Kinase Activity Assay. *Nanoscale* **2016**, *8*, 11649−11657.

(10) Yi, F.; Huang, X.; Ren, J. Simple and Sensitive Method for Determination of Protein Kinase Activity Based on Surface Charge Change of Peptide-Modified Gold Nanoparticles As Substrates. *Anal. Chem.* **2018**, *90*, 3871−3877.

(11) Wang, L.-j.; Yang, Y.; Zhang, C.-y. Phosphorylation-Directed Assembly of a Single Quantum Dot Based Nanosensor for Protein Kinase Assay. *Anal. Chem.* **2015**, *87*, 4696−4703.

(12) Watabe, T.; Terai, K.; Sumiyama, K.; Matsuda, M. Booster, a Red-Shifted Genetically Encoded Förster Resonance Energy Transfer (FRET) Biosensor Compatible with Cyan Fluorescent Protein/Yellow Fluorescent Protein-Based FRET Biosensors and Blue Light-Responsive Optogenetic Tools. *ACS Sens.* **2020**, *5*, 719−730.

(13) Liu, J.; Cheng, H.; He, D.; He, X.; Wang, K.; Liu, Q.; Zhao, S.; Yang, X. Label-Free Homogeneous Electrochemical Sensing Platform for Protein Kinase Assay Based on Carboxypeptidase Y-Assisted Peptide Cleavage and Vertically Ordered Mesoporous Silica Films. *Anal. Chem.* **2017**, *89*, 9062−9068.

(14) Lv, Y.; Chen, S.; Shen, Y.; Ji, J.; Zhou, Q.; Liu, S.; Zhang, Y. Competitive Multiple-Mechanism-Driven Electrochemiluminescent Detection of 8-Hydroxy-2′-deoxyguanosine. *J. Am. Chem. Soc.* **2018**, *140*, 2801−2804.

(15) Park, S. H.; Ko, K.-C.; Gwon, H. J. Feasibility Studies on a Protein Kinase Assay When Using Radioisotope Detection Technique for Developing a Protein Biochip. *J. Labelled Compd. Radiopharm.* **2007**, *50*, 724−728.

(16) Cho, Y.-L.; Kim, Y.-P.; Son, J. G.; Son, M.; Lee, T. G. On-Chip Peptide Mass Spectrometry Imaging for Protein Kinase Inhibitor Screening. *Anal. Chem.* **2017**, *89*, 799−806.

(17) Li, T.; Liu, D.; Wang, Z. Microarray-Based Raman Spectroscopic Assay for Kinase Inhibition by Gold Nanoparticle Probes. *Biosens. Bioelectron.* **2009**, *24*, 3335−3339.

(18) Wu, S.; Kong, X.-J.; Cen, Y.; Yu, R.-Q.; Chu, X. Phosphorylation-Induced Formation of a Cytochrome C-Peptide Complex: A Novel Fluorescent Sensing Platform for Protein Kinase Assay. *Chem. Commun.* **2016**, *52*, 776−779.

(19) Zhang, L.; Song, W.; Liang, R.-P.; Qiu, J.-D. Simultaneous Determination of Protein Kinase A and Casein Kinase II by Dual-Color Peptide Biomineralized Metal Nanoclusters. *Anal. Chem.* **2016**, *88*, 11460−11467.

(20) Zhou, J.; Xu, X.; Liu, X.; Li, H.; Nie, Z.; Qing, M.; Huang, Y.; Yao, S. A Gold Nanoparticles Colorimetric Assay for Label-Free

Detection of Protein Kinase Activity Based on Phosphorylation Protection Against Exopeptidase Cleavage. *Biosens. Bioelectron.* **2014**, *53*, 295−300.
(21) Shin, I.-S.; Chand, R.; Lee, S. W.; Rhee, H.-W.; Kim, Y.-S.; Hong, J.-I. Homogeneous Electrochemical Assay for Protein Kinase Activity. *Anal. Chem.* **2014**, *86*, 10992−10995.
(22) Liu, Z.; Qi, W.; Xu, G. Recent Advances in Electrochemiluminescence. *Chem. Soc. Rev.* **2015**, *44*, 3117−3142.
(23) Zhang, J.; Jin, R.; Jiang, D.; Chen, H.-Y. Electrochemiluminescence-Based Capacitance Microscopy for Label-Free Imaging of Antigens on the Cellular Plasma Membrane. *J. Am. Chem. Soc.* **2019**, *141*, 10294−10299.
(24) Zhao, H.-F.; Liang, R.-P.; Wang, J.-W.; Qiu, J.-D. A Dual-Potential Electrochemiluminescence Ratiometric Approach Based on Graphene Quantum Dots and Luminol for Highly Sensitive Detection of Protein Kinase Activity. *Chem. Commun.* **2015**, *51*, 12669−12672.
(25) Liu, J.; He, X.; Wang, K.; He, D.; Wang, Y.; Mao, Y.; Shi, H.; Wen, L. A highly Sensitive Electrochemiluminescence Assay for Protein Kinase Based on Double-Quenching of Graphene Quantum Dots by G-quadruplex−Hemin and Gold Nanoparticles. *Biosens. Bioelectron.* **2015**, *70*, 54−60.
(26) Jiang, X.; Wang, Z.; Wang, H.; Zhuo, Y.; Yuan, R.; Chai, Y. A Novel Metal−Organic Framework Loaded with Abundant N-(aminobutyl)-N-(ethylisoluminol) as a High-efficiency Electrochemiluminescence Indicator for Sensitive Detection of Mucin1 on Cancer Cells. *Chem. Commun.* **2017**, *53*, 9705−9708.
(27) Huang, X.; Deng, X.; Qi, W.; Wu, D. Highly Sensitive Luminol Electrochemiluminescence Immunosensor Based on Platinum-Gold Alloy Hybrid Functionalized Zinc Oxide Nanocomposites for Catalytic Amplification. *Sens. Actuators, B* **2018**, *273*, 466−472.
(28) Zhang, G.-Y.; Deng, S.-Y.; Zhang, X.-J.; Shan, D. Cathodic Electrochemiluminescence of Singlet Oxygen Induced by the Electroactive Zinc Porphyrin in Aqueous Media. *Electrochim. Acta* **2016**, *190*, 64−68.
(29) Pu, G.; Zhang, D.; Mao, X.; Zhang, Z.; Wang, H.; Ning, X.; Lu, X. Biomimetic Interfacial Electron-Induced Electrochemiluminesence. *Anal. Chem.* **2018**, *90*, 5272−5279.
(30) Pu, G.; Yang, Z.; Wu, Y.; Wang, Z.; Deng, Y.; Gao, Y.; Zhang, Z.; Lu, X. Investigation into the Oxygen-Involved Electrochemiluminescence of Porphyrins and Its Regulation by Peripheral Substituents/Central Metals. *Anal. Chem.* **2019**, *91*, 2319−2328.
(31) Zhou, Q.; Li, G.; Chen, K.; Yang, H.; Yang, M.; Zhang, Y.; Wan, Y.; Shen, Y.; Zhang, Y. Simultaneous Unlocking Optoelectronic and Interfacial Properties of C60 for Ultrasensitive Immunosensing by Coupling to Metal−Organic Framework. *Anal. Chem.* **2020**, *92*, 983−990.
(32) Zhang, G.; Shan, D.; Dong, H.; Cosnier, S.; Al-Ghanim, K. A.; Ahmad, Z.; Mahboob, S.; Zhang, X. DNA-Mediated Nanoscale Metal−Organic Frameworks for Ultrasensitive Photoelectrochemical Enzyme-Free Immunoassay. *Anal. Chem.* **2018**, *90*, 12284−12291.
(33) Zhang, G.-Y.; Zhuang, Y.-H.; Shan, D.; Su, G.-F.; Cosnier, S.; Zhang, X.-J. Zirconium-Based Porphyrinic Metal−Organic Framework (PCN-222): Enhanced Photoelectrochemical Response and Its Application for Label-Free Phosphoprotein Detection. *Anal. Chem.* **2016**, *88*, 11207−11212.
(34) Zhang, G.; Chai, H.; Tian, M.; Zhu, S.; Qu, L.; Zhang, X. Zirconium−Metalloporphyrin Frameworks−Luminol Competitive Electrochemiluminescence for Ratiometric Detection of Polynucleotide Kinase Activity. *Anal. Chem.* **2020**, *92*, 7354−7362.
(35) Peng, Y.; Li, Y.; Ban, Y.; Yang, W. Two-Dimensional Metal−Organic Framework Nanosheets for Membrane-Based Gas Separation. *Angew. Chem., Int. Ed.* **2017**, *56*, 9757−9761.
(36) Cao, L.; Lin, Z.; Peng, F.; Wang, W.; Huang, R.; Wang, C.; Yan, J.; Liang, J.; Zhang, Z.; Zhang, T.; Long, L.; Sun, J.; Lin, W. Self-Supporting Metal−Organic Layers as Single-Site Solid Catalysts. *Angew. Chem., Int. Ed.* **2016**, *55*, 4962−4966.
(37) Zhao, M.; Huang, Y.; Peng, Y.; Huang, Z.; Ma, Q.; Zhang, H. Two-Dimensional Metal−Organic Framework Nanosheets: Synthesis and Applications. *Chem. Soc. Rev.* **2018**, *47*, 6267−6295.
(38) Zhao, M.; Wang, Y.; Ma, Q.; Huang, Y.; Zhang, X.; Ping, J.; Zhang, Z.; Lu, Q.; Yu, Y.; Xu, H.; Zhao, Y.; Zhang, H. Ultrathin 2D Metal−Organic Framework Nanosheets. *Adv. Mater.* **2015**, *27*, 7372−7378.
(39) Xu, G.; Otsubo, K.; Yamada, T.; Sakaida, S.; Kitagawa, H. Superprotonic Conductivity in a Highly Oriented Crystalline Metal−Organic Framework Nanofilm. *J. Am. Chem. Soc.* **2013**, *135*, 7438−7441.
(40) Zhao, Y.; Wang, J.; Pei, R. Micron-Sized Ultrathin Metal−Organic Framework Sheet. *J. Am. Chem. Soc.* **2020**, *142*, 10331−10336.
(41) Rochford, J.; Chu, D.; Hagfeldt, A.; Galoppini, E. Tetrachelate Porphyrin Chromophores for Metal Oxide Semiconductor Sensitization: Effect of the Spacer Length and Anchoring Group Position. *J. Am. Chem. Soc.* **2007**, *129*, 4655−4665.
(42) Makiura, R.; Motoyama, S.; Umemura, Y.; Yamanaka, H.; Sakata, O.; Kitagawa, H. Surface Nano-Architecture of a Metal−Organic Framework. *Nat. Mater.* **2010**, *9*, 565−571.
(43) Li, X.; Zhang, G.; Bai, X.; Sun, X.; Wang, X.; Wang, E.; Dai, H. Highly Conducting Graphene Sheets and Langmuir−Blodgett films. *Nat. Nanotechnol.* **2008**, *3*, 538−542.
(44) Wang, Y.; Zhao, M.; Ping, J.; Chen, B.; Cao, X.; Huang, Y.; Tan, C.; Ma, Q.; Wu, S.; Yu, Y.; Lu, Q.; Chen, J.; Zhao, W.; Ying, Y.; Zhang, H. Bioinspired Design of Ultrathin 2D Bimetallic Metal−Organic-Framework Nanosheets Used as Biomimetic Enzymes. *Adv. Mater.* **2016**, *28*, 4149−4155.
(45) Röder, R.; Preiß, T.; Hirschle, P.; Steinborn, B.; Zimpel, A.; Höhn, M.; Rädler, J.-O.; Bein, T.; Wagner, E.; Wuttke, S.; Lächelt, U. Multifunctional Nanoparticles by Coordinative Self-assembly of His-Tagged Units with Metal−Organic Frameworks. *J. Am. Chem. Soc.* **2017**, *139*, 2359−2368.
(46) Zhao, Y.; Dong, Y.; Lu, F.; Ju, C.; Liu, L.; Zhang, J.; Zhang, B.; Feng, Y. Coordinative Integration of a Metal-Porphyrinic Framework and TiO_2 Nanoparticles for the Formation of Composite Photocatalysts with Enhanced Visible-Light-Driven Photocatalytic Activities. *J. Mater. Chem. A* **2017**, *5*, 15380−15389.
(47) Cozza, G.; Bonvini, P.; Zorzi, E.; Poletto, G.; Pagano, M. A.; Sarno, S.; Donella-Deana, A.; Zagotto, G.; Rosolen, A.; Pinna, L. A.; Meggio, F.; Moro, S. Identification of Ellagic Acid as Potent Inhibitor of Protein Kinase CK2: A Successful Example of a Virtual Screening Application. *J. Med. Chem.* **2006**, *49*, 2363−2366.
(48) Wang, Z.; Sun, N.; He, Y.; Liu, Y.; Li, J. DNA Assembled Gold Nanoparticles Polymeric Network Blocks Modular Highly Sensitive Electrochemical Biosensors for Protein Kinase Activity Analysis and Inhibition. *Anal. Chem.* **2014**, *86*, 6153−6159.

https://dx.doi.org/10.1021/acsabm.0c01453
ACS Appl. Bio Mater. 2021, 4, 1616−1623